Symmetry breaking induced anti-resonance in three dimensional sub-diffraction semiconducting grating

F. Cheng, B. H. Li, J. Han, H. Xiao, C. Z. Gu et al.

Citation: Appl. Phys. Lett. **102**, 151113 (2013); doi: 10.1063/1.4802726
View online: http://dx.doi.org/10.1063/1.4802726
View Table of Contents: http://apl.aip.org/resource/1/APPLAB/v102/i15
Published by the American Institute of Physics.

Symmetry breaking induced anti-resonance in three dimensional sub-diffraction semiconducting grating

F. Cheng, B. H. Li, J. Han, H. Xiao, C. Z. Gu, and X. G. Qiu[a)]
Beijing National Laboratory for Condensed Matter Physics, Institute of Physics, Chinese Academy of Sciences, P.O. Box 603, Beijing 100190, China

(Received 6 March 2013; accepted 5 April 2013; published online 19 April 2013)

A kind of three dimensional, sub-diffraction grating with converging-diverging channel working at terahertz regime has been developed on doped silicon wafers by wet etching. By introducing a geometric asymmetry to the vertical direction of the 3D grating, an anti-resonance is observed near the resonant wavelength of the surface plasmon polariton mode. Numerical simulations reveal that the surface waves propagating on the top and bottom surfaces are decoupled due to the symmetry breaking, which results in the destructive interference of electromagnetic field and thus the anti-resonance in the spectrum. It was also found that the bulk sensitivity of the 3D structure as a terahertz sensor can reach a value up to 8818%/RIU and a figure of merit up to 50.
 [http://dx.doi.org/10.1063/1.4802726]

The discovery of enhanced optical transmission (EOT) through subwavelength hole arrays (MHAs) perforated on metal films by Ebbesen *et al.*[1] has inspired renewed interest in the artificial manipulation of light beyond the diffraction limit. Generally, EOT is believed to be assisted by the resonant excitation of surface plasmon polaritons (SPPs) at the metal-dielectric interface, which has been explored extensively[2–7] and expected to be utilized in near-field imaging,[8] photolithography,[9] bio-sensing,[10] and so on. For all these applications, it is of great interest to provide devices with large tunability on the excitation and guiding of SPPs.[11]

To achieve this goal, various approaches have been employed such as geometrical modification[12–15] and modulating the property of supporting materials[16,17] of SPPs. As compared to metals, semiconductors such as silicon (Si)[18,19] or indium antimonide (InSb)[20] facilitate the active manipulation of plasmonic devices since the carrier concentration can be modified by control of temperature[21,22] or photoirradiation.[19,23,24] Moreover, semiconductors can be processed easily and economically, which is of crucial importance for future generalization and application of plasmonic devices.[25,26] In this letter, we report that by employing the wet etching technique for processing semiconductors such as Si, a kind of free-standing, three dimensional (3D) gratings working at terahertz (THz) frequency were fabricated. We demonstrate experimentally and numerically that not only an additional degree of freedom for geometrical modulation was provided by this kind of structures, but also high bulk sensitivity and large value of figure of merit (FoM) can be achieved in the THz surface plasmon resonance (SPR) sensor.

The samples were processed from a commercially available 200 μm-thick n-type Si wafer with a quoted resistivity (ρ) smaller than 0.01 $\Omega \cdot$ cm. The permittivity of doped semiconductors can be well described by the Drude model at THz frequencies in the absence of interband transitions,

$$\varepsilon(\omega) = \varepsilon_{static} - \frac{{\omega_p}^2}{\omega^2 + \tau^{-2}} + i\frac{{\omega_p}^2\tau^{-1}}{\omega(\omega^2 + \tau^{-2})}, \qquad (1)$$

where ε_{static} is the background dielectric constant which has a value about 12 for silicon at THz regime,[27] τ is the average collision time of electrons, and $\omega_p = \sqrt{Ne^2/\varepsilon_0 m^*}$ is the plasma frequency with N, e, ε_0, and m^* being the doping concentration, fundamental charge, vacuum permittivity, and electron effective mass ($m^* = 0.27m_0$ for n-type Si, where m_0 is the mass of the free electron[28]), respectively. From Hall measurements, the carrier density of the wafer was estimated to be $1.1 \times 10^{19}\text{cm}^{-3}$ at room temperature, so the corresponding plasma frequency $\omega_p/2\pi \approx 60$ THz and the electron mobility $\mu = \tau e/m^* \approx 110\,\text{cm}^2/\text{Vs}$.[29] With Eq. (1), it can be estimated that the permittivity of doped Si studied here approximates to be $-27 + 369\,i$ at 1 THz.

Starting from a double-side polished Si(100) wafer, a 200 nm-thick high-quality Si_3N_4 mask layer was deposited on both sides using plasma enhanced chemical vapor deposition (PECVD) at 380 °C. The desired patterns on mask layer were obtained by ultra-violet lithography and reactive ion etching (RIE). Then the exposed Si area was wet etched in a 5 wt. % tetramethylammonium hydroxide (TMAH) water solution dual doped with silicic acid (SA) and ammonium peroxodisulphate (AP) at 80 °C for about 3 h.[30] Finally, the remaining Si_3N_4 mask layer was removed by RIE to reveal the desired free-standing, pyramidal converging channel (CC, converging angle $\theta \approx 54.7°$). Figs. 1(a)–1(c) show the scanning electron microscope (SEM) images of the gratings. Furthermore, by employing the bottom microscope alignment process, the same grating on the bottom of the wafer can be patterned, forming a 3D grating with symmetrical converging-diverging channels (CDCs, Fig. 1(d)). Compared to the conventional dry etching process, the anisotropic wet etching provides an inexpensive, time-saving and defects-remedying method to get high aspect ratio structures and ultra-smooth side walls which can significantly reduce the

a)xgqiu@aphy.iphy.ac.cn

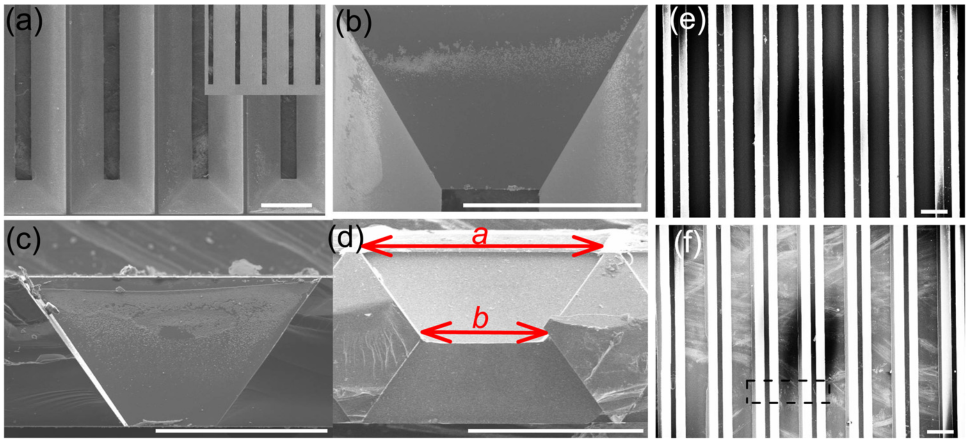

FIG. 1. SEM images of the samples. (a) Top view of a grating with converging slit wet etched on the free-standing Si wafer. (Inset: bottom view) (b) Oblique and (c) side view of the converging slit. (d) Side view of a CDC. (e) Top view of sample 1 with symmetrical CDC (period $L = 350\,\mu$m, slit width $a = 300\,\mu$m, $b = 160\,\mu$m). (f) Top view of sample 2 with asymmetrical CDC (period $L = 350\,\mu$m, $a = 310\,\mu$m, $b = 170\,\mu$m. A megascopic area in the dashed box is shown in the inset of Fig. 3 (a)), Scale bar: 200 μm.

propagation loss of surface waves.[31,32] This sub-diffraction grating provides an extra degree of geometrical variable perpendicular to the 2D plane, which makes it possible for us to explore in detail the light tunneling through the apertures as well as the coupling effect between surface waves propagating on opposite sides.

A Fourier transform infrared spectrometer (ABB BOMEM DA8) was used for the study of THz transmission through the sub-wavelength structures. At normal incidence and under TM polarization (magnetic-field vector parallel to the slits), the resonant wavelengths for the excitation of SPPs on a 1D grating are approximately given by

$$\lambda_{sp}^{m,n} = \frac{L}{m}\sqrt{\frac{\varepsilon_1\varepsilon_2}{\varepsilon_1+\varepsilon_2}}, \tag{2}$$

where L is the lattice constant, m and n are the integer mode indices, and $\varepsilon_i (i = 1, 2)$ are the dielectric constants of the surrounding materials. We found that transmission signal of CC samples is too weak to be detected by the bolometer but that of the grating with CDCs is much higher, which agrees well with the simulation by Battula *et al.*[33]

Figure 2(a) shows the zero-order transmission of sample 1 (top view shown in Fig. 1(e)) under TM polarization. A remarkable resonance showing Fano-like profile (black solid) observed around 450 μm can be indexed as the $(\pm1, 0)$ mode according to Eq. (2). The resonant feature at about 230 μm emerging as a platform is assigned to the $(\pm2, 0)$ mode and that at about 140 μm to the higher order $(\pm3, 0)$ mode, which are separated from each other by a Wood's anomaly. To compare with its metallic counterpart, we evaporated a layer of 100 nm gold on the top side of the grating and found that the transmission lineshape (red solid) remains unchanged except a $\sim$7% increase in magnitude. As another 100 nm thick gold layer was evaporated on the bottom side, the transmittance increases almost the same magnitude as above (blue solid and inset). We attribute the enhanced transmittance to the fact that the higher free carrier density of gold (6×10^{22} cm^{-3}) introduces smaller scattering losses of surface waves owing to the reduced evanescent decay length of the electric field into the metal.[34] The observed phenomenon is analogous to the crescent transmission when the two interfaces of Si slit-groove structure were photo-excited independently or simultaneously with laser pulses.[23]

To better evaluate the transmission properties, numerical modeling using finite element method (FEM) was carried out for perfect electric conductor (PEC) structures which have the

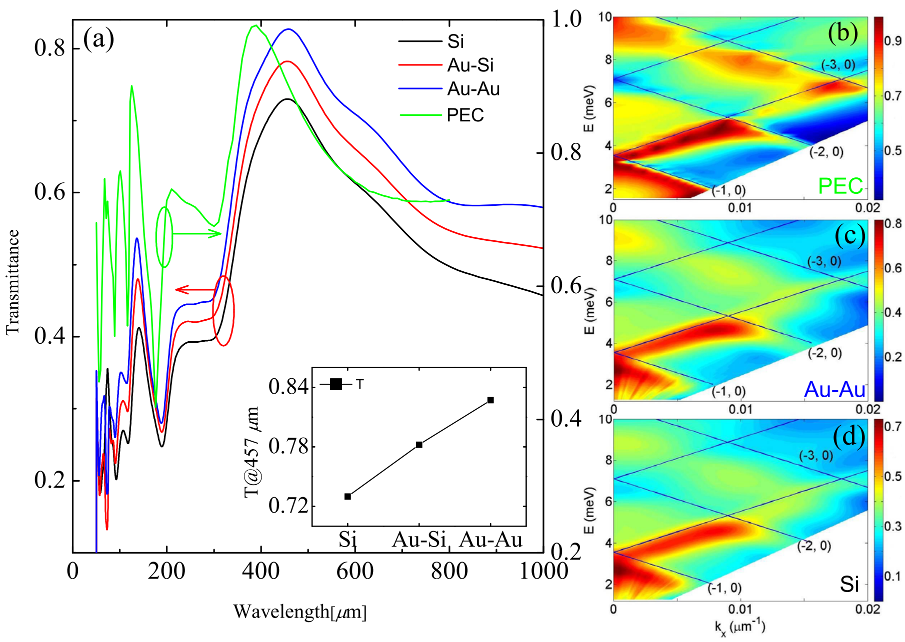

FIG. 2. (a) Zero-order transmission spectra of sample 1 (Black, red and blue solid are experimental results of Si, Au-Si, and Au-Au structures and green solid the simulation curve of PEC. Inset: Peak intensity of the $(\pm1, 0)$ mode for different structures). (b-d) The angle-dependent transmission contour maps for PEC, Au-Au, and Si structures, respectively. Theoretical SPP bands (blue solid) are superposed on the maps, with different SPP modes indexed by (m, n).

same geometrical parameters as sample 1 (resonant features observed here are geometrically induced surface EM modes that mimic the behavior of SPPs in metal at visible regime). The main characteristics of the transmission spectrum are well reproduced by the simulation curve (green solid in Fig. 2(a)), which verifies the rationality to substitute doped Si with PEC in simulation. The angle-dependent transmission was also constructed for comparison with Si and gold structures, reflecting the dispersion relation of SPPs (Figs. 2(b)–2(d)).

The 3D nature of the grating enables us to further explore the geometrical modulation on the propagation of SPPs on the structures and thus help us to understand the physics related to EOT. To this end, we introduce for sample 2 (top view shown in Fig. 1(f)) an asymmetry[35] by shifting horizontally the converging channel with respect to the diverging channel as shown in the inset of Fig. 3(a). Surprisingly, a shift (s) of 25 μm results in a depression of the original resonant peak and the appearance of a minimum of transmittance near the wavelength of ($\pm$1, 0) mode. We have also deposited gold on the top converging channel only or on both the top and bottom channels: the transmission dip remains in all cases although the transmittance increases as what is observed for sample 1.

To better illustrate the symmetry breaking induced transformation from peak to dip in transmission, we plot in Fig. 3(a) the modeled transmission curves of sample 2 (green solid) and the one without shift (purple dashed). The former captures the features of experimental result: the resonant peak of ($\pm$1, 0) mode disappears and a sharp anti-resonance emerges at the wavelength which locates the transmission peak of the latter. Simulations also reveal that by changing only the thickness of the grating, the location of this anti-resonance can be tuned, which transfers from the red side of ($\pm$1, 0) mode for thinner grating to blue side for thicker ones (data not shown), suggesting that the Fano resonance observed here is spectrally tunable which is similar to those observed in an array of nano-antennas.[36]

To further explore the evolution of the anti-resonance with the degree of asymmetry characterized by the shift (s) between the converging and the diverging channels, we have carried out a series of numerical simulations for gratings with s ranging from 5 to 37.5 μm. As can be appreciated from Fig. 3(b)), a larger s introduces a deeper and wider anti-resonance. The modulation depth D (defined as the transmittance decline at the minimum for asymmetric gratings from the transmission maximum of the symmetric one with $s = 0$ (horizontal red dashed)) follows a good linear relation (Fig. 3(c)) with s, evolving from $D \sim 4\%$ for $s = 5$ μm to $D \sim 84\%$ for $s = 37.5$ μm.

To understand the origin of the asymmetry induced anti-resonance, we calculate the electric field distribution at the extreme points noted by arrows in Figs. 4(a) and 4(e). For the symmetric grating without shift, there exist two transmission channels: the direction THz transmission through the slit ($\lambda_{\pm 1,0} \approx 2b$) associated possibly with a cavity mode which is illustrated by the distribution of E_x component shown in Fig. 4(c) and the resonant transmission assisted by SPPs illustrated by the E_z component shown in Fig. 4(d).

From the field distribution of E_z, we can see that the SPPs on the top and bottom surfaces oscillate in-phase and that the field strength along the slopes is relatively large, suggesting that the coupling between SPPs on the top and bottom surfaces are well established due to the mirror symmetry structure. The Fano line shape of the ($\pm$1, 0) mode shown in Fig. 4(a)) is just a result of the interference between these two transmission channels.

For the asymmetric structure with $s = 25$ μm in sample 2, however, the situation is quite another story at the same wavelength. The field distribution is significantly changed by the symmetry-breaking of CDC, as shown in Figs. 4(f)–4(h). Unlike the former case where SPPs can be excited and propagate on the converging and diverging slopes constructively, E_z focuses mainly at the horizontal narrow ridges of the grating and diminishes dramatically along the slopes (Figs. 4(f) and 4(h)), from which we can infer that the SPP modes become more tangent to the horizontal surfaces and the evanescent coupling between them was blocked by the geometric discontinuity. In parallel, we noted that the E_x component

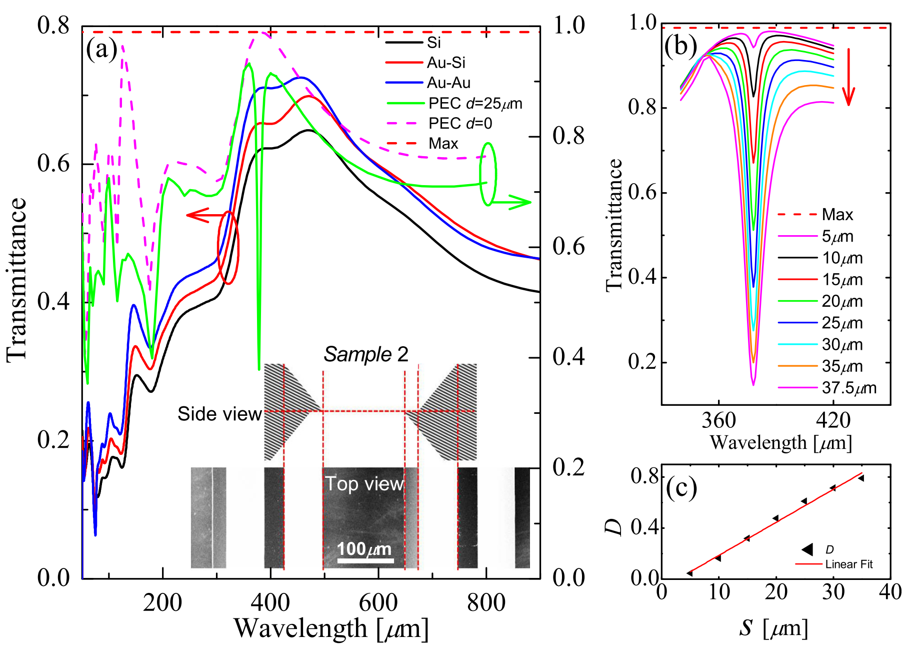

FIG. 3. (a) Zero-order transmission spectra of sample 2 (Inset: schematic plot of side view and SEM image of top view of a CDC with a shift $s = 25$ μm, cf. Fig. 1(f)). Black, red, and blue solid lines are experimental results of Si, Au-Si and Au-Au sturctures; green solid is the simulation curve and purple solid the one without shift. (b) The simulated anti-resonance for different shifts ($s = 5 \sim 37.5$ μm), the red dashed line represents the transmission maximum of sample without shift. (c) The modulation depth variation as a function of s.

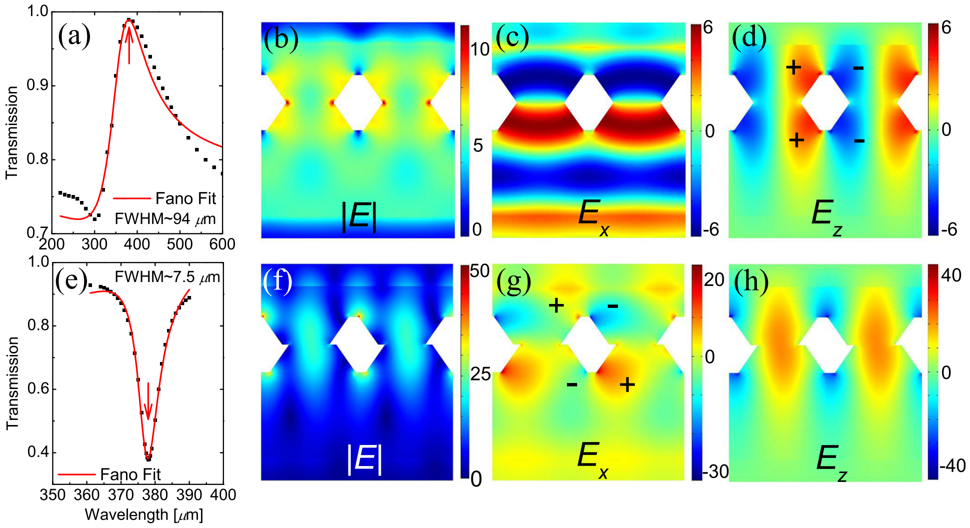

FIG. 4. (a) Simulated data (dot) and Fano fitting curve (red solid) of the ($\pm$1,0) mode for a grating with symmetric CDC which has the same geometrical parameter with sample 2. (b-d) $|\vec{E}|$, E_x, and E_z distribution at the resonant wavelength. The E_y component is negligible compared to other components. (e) Simulated data (dot) and Fano fitting curve (red solid) of the anti-resonance for sample 2. (f-h) $|\vec{E}|$, E_x and E_z distribution at the anti-resonant dip (Unit: V/m).

focuses on the top and bottom edges of CDC with opposite signs (Fig. 4(g)), originating from different charge accumulation in the multiple scattering of SPP modes on the protruding shifts. The opposite field distribution demonstrates that the surface wave propagating on the bottom side of CDC grating is decoupled to that propagating on the top side. Consequently, a narrow asymmetric Fano anti-resonance can be observed at the resonant wavelength of the ($\pm$1, 0) mode. We note that in another kind of asymmetric metallic grating working at microwave frequency, a sharp, Fano-like phase resonance can also be supported due to the interference between Fabry-Perot-like modes and diffractively coupled surface waves.[37] In this way, the optical response of symmetry-breaking, 3D structures deserves to be further explored from both the fundamental and application points of view.

It is noteworthy that the full width at half maximum (FWHM) of the anti-resonant dip approximates only 7.5 μm (according to Fano fit shown in Fig. 4(e)), which is much smaller than that of the ($\pm$1, 0) mode of a symmetric structure ($\sim$94μm according to Fano fit shown in Fig. 4(a)). This small value of FWHM suggests us that the asymmetrical 3D sub-diffraction grating can be utilized as SPR sensor in THz region. To evaluate the bulk sensitivity of the asymmetric grating, we plot in Fig. 5(a) the calculated anti-resonant dip of sample 2 at different dielectric environment. As could be expected, the resonant wavelength red-shifts linearly as the surrounding refractive index (RI) increases, and the slope of

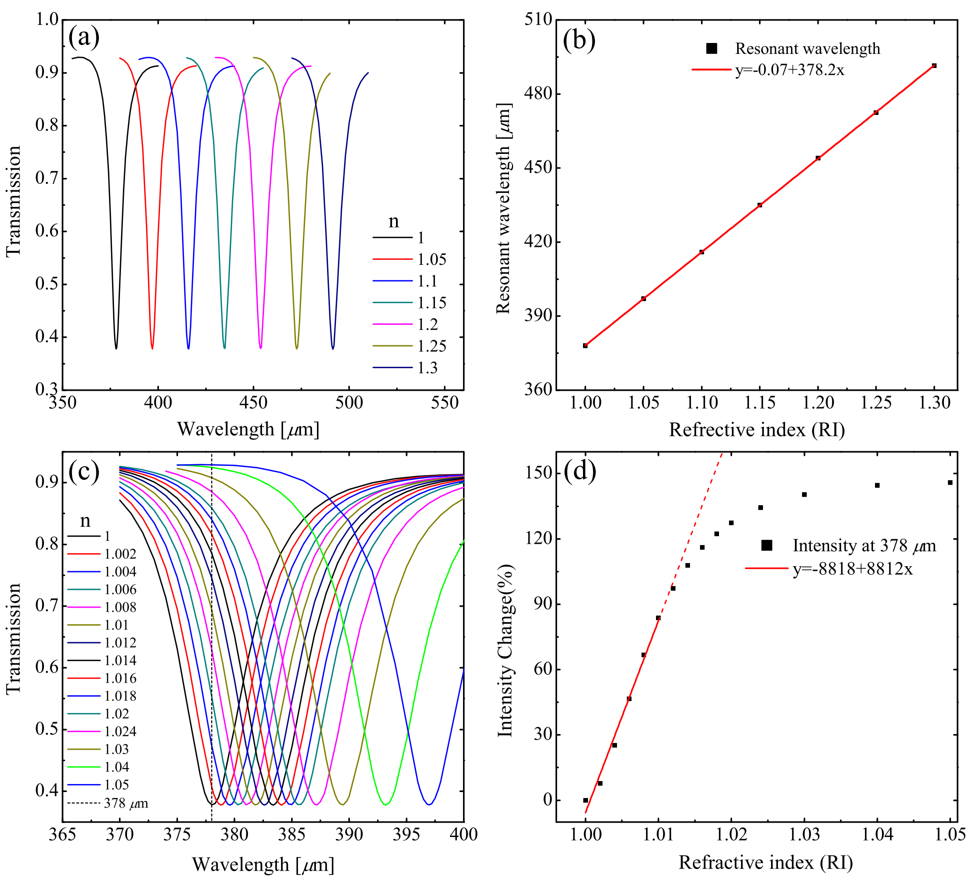

FIG. 5. (a) Simulated anti-resonance of sample 2 at different dielectric environment. (b) Resonant wavelength versus the RI of surrounding medium. The slope of the fitting curve shows the wavelength sensitivity. (c) Simulated anti-resonance for a small change of RI (0.05) of the surrounding medium. (d) Intensity change versus RI of surrounding medium at 378 μm. The slope of the fitting curve shows the intensity sensitivity.

the linear fitting curve (red solid in Fig. 5(b)) shows that the wavelength sensitivity ($\triangle\lambda/\triangle$n) is 378.2 μm RIU^{-1}, which approaches that of the polymer fiber-based SP-like THz sensor (simulated spectral sensitivity $S_\lambda = 400\,\mu\text{m/RIU}$).[38] Accordingly, the figure of merit (FoM, defined as ($\triangle\lambda/\triangle$n)/FWHM) approximates 50.4, which is comparable with that of the 2D nanostructure-based SPR sensor (FoM of 55)[39] and nanoparticle-based localized surface plasmon resonance (LSPR) sensor (FoM of 10.6).[40]

For real-time and high-throughput sensing, the intensity sensitivity (defined as $(\triangle I/I_0)/\triangle n$) is often employed to evaluate the sensing ability.[41] Figure 5(c) presents the calculated anti-resonant dip of sample 2 with the surrounding refractive index increases from 1 to 1.05. We examined the intensity change at 378 μm as the dip red-shifts about 20 μm: the transmission intensity increases linearly as the refractive index changes from 1 to 1.012 and then tends to saturation when the refractive index reaches 1.04 (Fig. 5(d)). The slope of the linear fitting curve shows that bulk intensity sensitivity of this CDG can reach about 8812%/RIU, which is comparable with the measured intensity sensitivity 10 367%/RIU in the visible regime.[39]

Through the above analysis, we emphasize that the 3D grating provides a platform where the evanescent coupling of surface waves can be manipulated, which benefits a precise engineering of the Fano line shape. Meanwhile, the anti-resonant feature of asymmetric gratings can be utilized in high-performance SPR sensors with high bulk sensitivity and FoM. We anticipate that the proposed 3D structures patterned on doped semiconductors can serve as a viable recruitment of metallic counterparts and be integrated with the existing Si based electronic devices. Further optimization and extension cannot only opens the way for the realization of semiconductor-based metamaterials but also facilitate the integration of plasmonics and nanophotonics, stimulating the development of opto-electronic devices such as modulators and integrated circuits.

We acknowledge Professor Javier Aizpurua for helpful discussion. This work is supported by National Basic Research Program of China (2009CB929102, 2011CBA00107, 2012CB921302), National Science Foundation of China (No. 10974241, 91121004), and the Knowledge Innovation Program of CAS (No. KJCX2-EW-W02).

[1]T. W. Ebbesen, H. J. Lezec, H. F. Ghaemi, T. Thio, and P. A. Wolff, Nature(London) **391**, 667 (1998).
[2]E. Popov, M. Neviere, S. Enoch, and R. Reinisch, Phys. Rev. B **62**, 16100 (2000).
[3]L. Martin-Moreno, F. J. Garcia-Vidal, H. J. Lezec, K. M. Pellerin, T. Thio, J. B. Pendry, and T. W. Ebbesen, Phys. Rev. Lett. **86**, 1114 (2001).
[4]W. L. Barnes, W. A. Murray, J. Dintinger, E. Devaux, and T. W. Ebbesen, Phys. Rev. Lett. **92**, 107401 (2004).
[5]X. Fang, Z. Li, Y. Long, H. Wei, R. Liu, J. Ma, M. Kamran, H. Zhao, X. Han, B. Zhao *et al.*, Phys. Rev. Lett. **99**, 066805 (2007).
[6]R. F. Oulton, V. J. Sorger, T. Zentgraf, R.-M. Ma, C. Gladden, L. Dai, G. Bartal, and X. Zhang, Nature **461**, 629 (2009).
[7]F. Cheng, H. F. Liu, B. H. Li, J. Han, H. Xiao, X. F. Han, C. Z. Gu, and X. G. Qiu, Appl. Phys. Lett. **100**, 131110 (2012).
[8]N. Fang, H. Lee, C. Sun, and X. Zhang, Science **308**, 534 (2005).
[9]Z. Liu, Q. Wei, and X. Zhang, Nano Lett. **5**, 957 (2005).
[10]M. Najiminaini, F. Vasefi, B. Kaminska, and J. J. L. Carson, Appl. Phys. Lett. **100**, 063110 (2012).
[11]C. R. Williams, S. R. Andrews, S. A. Maier, A. I. Fernandez-Dominguez, L. Martin Moreno, and F. J. Garcia-Vidal, Nat. Photonics **2**, 175 (2008).
[12]K. J. K. Koerkamp, S. Enoch, F. B. Segerink, N. F. van Hulst, and L. Kuipers, Phys. Rev. Lett. **92**, 183901 (2004).
[13]C. Janke, J. G. Rivas, C. Schotsch, L. Beckmann, P. H. Bolivar, and H. Kurz, Phys. Rev. B **69**, 205314 (2004).
[14]Y. Li, J. Pan, P. Zhan, S. Zhu, N. Ming, Z. Wang, W. Han, X. Jiang, and J. Zi, Opt. Express **18**, 3546 (2010).
[15]J.-C. Yang, H. Gao, J. Y. Suh, W. Zhou, M. H. Lee, and T. W. Odom, Nano Lett. **10**, 3173 (2010).
[16]T. Thio, H. Ghaemi, H. Lezec, P. Wolff, and T. Ebbesen, J. Opt. Soc. Am. B-Opt. Phys. **16**, 1743 (1999).
[17]S. M. Williams, A. D. Stafford, K. R. Rodriguez, T. M. Rogers, and J. V. Coe, J. Phys. Chem. B **107**, 11871 (2003).
[18]J. Gómez Rivas, C. Schotsch, P. Haring Bolivar, and H. Kurz, Phys. Rev. B **68**, 201306 (2003).
[19]W. Zhang, A. K. Azad, J. Han, J. Xu, J. Chen, and X.-C. Zhang, Phys. Rev. Lett. **98**, 183901 (2007).
[20]C. Janke, J. G. Rivas, P. H. Bolivar, and H. Kurz, Opt. Lett. **30**, 2357 (2005).
[21]J. G. Rivas, M. Kuttge, H. Kurz, P. H. Bolivar, and J. A. Sanchez-Gil, Appl. Phys. Lett. **88**, 082106 (2006).
[22]J. Han, A. Lakhtakia, Z. Tian, X. Lu, and W. Zhang, Opt. Lett. **34**, 1465 (2009).
[23]E. Hendry, F. J. Garcia-Vidal, L. Martin-Moreno, J. G. Rivas, M. Bonn, A. P. Hibbins, and M. J. Lockyear, Phys. Rev. Lett. **100**, 123901 (2008).
[24]T. Okada, S. Tsuji, K. Tanaka, K. Hirao, and K. Tanaka, Appl. Phys. Lett. **97**, 261111 (2010).
[25]A. J. Hoffman, L. Alekseyev, S. S. Howard, K. J. Franz, D. Wasserman, V. A. Podolskiy, E. E. Narimanov, D. L. Sivco, and C. Gmachl, Nature Mater. **6**, 946 (2007).
[26]J. G. Rivas, M. Kuttge, P. H. Bolivar, H. Kurz, and J. A. Sánchez-Gil, Phys. Rev. Lett. **93**, 256804 (2004).
[27]R. Ulbricht, E. Hendry, J. Shan, T. F. Heinz, and M. Bonn, Rev. Mod. Phys. **83**, 543 (2011).
[28]E. D. Palik and D. F. Edwards, *Handbook of Optical Constants of Solids* (Academic Press Limited, 1985).
[29]C. Jacoboni, C. Canali, G. Ottaviani, and A. A. Quaranta, Solid-State Electron. **20**, 77 (1977).
[30]K. Biswas and S. Kal, Microelectron. J. **37**, 519 (2006).
[31]P. Nagpal, N. C. Lindquist, S.-H. Oh, and D. J. Norris, Science **325**, 594 (2009).
[32]B.-H. Li, C. E. Sanders, J. McIlhargey, F. Cheng, C. Gu, G. Zhang, K. Wu, J. Kim, S. H. Mousavi, A. B. Khanikaev *et al.*, Nano Lett. **12**, 6187 (2012).
[33]A. Battula, Y. Lu, R. J. Knize, K. Reinhardt, and S. Chen, Opt. Express **15**, 14629 (2007).
[34]J. A. Sánchez-Gil and J. G. Rivas, Phys. Rev. B **73**, 205410 (2006).
[35]F. Hao, Y. Sonnefraud, P. Van Dorpe, S. A. Maier, N. J. Halas, and P. Nordlander, Nano Lett. **8**, 3983 (2008).
[36]V. Giannini, Y. Francescato, H. Amrania, C. C. Phillips, and S. A. Maier, Nano Lett. **11**, 2835 (2011).
[37]H. J. Rance, O. K. Hamilton, J. R. Sambles, and A. P. Hibbins, Appl. Phys. Lett. **95**, 041905 (2009).
[38]A. Hassani and M. Skorobogatiy, Opt. Express **16**, 20206 (2008).
[39]K.-L. Lee, P.-W. Chen, S.-H. Wu, J.-B. Huang, S.-Y. Yang, and P.-K. Wei, ACS Nano **6**, 2931 (2012).
[40]N. A. Mirin, K. Bao, and P. Nordlander, J. Phys. Chem. A **113**, 4028 (2009).
[41]K.-L. Lee and P.-K. Wei, Appl. Phys. Lett. **99**, 083108 (2011).